

Public Domain Mark 1.0 Universal

This work was written as part of one of the author's official duties as an Employee of the United States Government and is therefore a work of the United States Government. In accordance with 17 U.S.C. 105, no copyright protection is available for such works under U.S. Law.

Access to this work was provided by the University of Maryland, Baltimore County (UMBC) ScholarWorks@UMBC digital repository on the Maryland Shared Open Access (MD-SOAR) platform.

Please provide feedback

Please support the ScholarWorks@UMBC repository by emailing scholarworks-group@umbc.edu and telling us what having access to this work means to you and why it's important to you. Thank you.



Comparative Analysis of Type III Radio Bursts and Solar Flares: Spatial Localization and Correlation with Solar Flare Intensity

Vratislav Krupar^{1,2}, Oksana Kruparova^{1,2}, Adam Szabo², Frantisek Nemec³, Milan Maksimovic⁴, Juan Carlos Martinez Oliveros⁵, David Lario², Xavier Bonnin⁴, Antonio Vecchio^{4,6}, Marc Pulupa⁵, and Stuart D. Bale^{5,7}

¹ Goddard Planetary Heliophysics Institute, University of Maryland, Baltimore County, Baltimore, MD 21250, USA; vratislav.krupar@nasa.gov

² Heliospheric Physics Laboratory, Heliophysics Division, NASA Goddard Space Flight Center, Greenbelt, MD 20771, USA

³ Faculty of Mathematics and Physics, Charles University, 121 16 Prague, Czech Republic

⁴ LESIA, Observatoire de Paris, Université PSL, CNRS, Sorbonne Université, Université de Paris, F-92195 Meudon, France

⁵ Space Sciences Laboratory, University of California, Berkeley, Berkeley, CA 94720, USA

⁶ Radboud Radio Lab, Department of Astrophysics/IMAPP-Radboud University, NL-6500 GL Nijmegen, The Netherlands

⁷ Physics Department, University of California, Berkeley, Berkeley, CA 94720, USA

Received 2023 April 3; revised 2023 November 14; accepted 2023 December 4; published 2024 January 17

Abstract

We present a comprehensive study of type III radio bursts and their association with solar flares of magnitude M1.0 and larger, as observed by four widely separated spacecraft (Parker Solar Probe, Solar Orbiter, STEREO-A, and Wind). Our main focus is the introduction and validation of two methods for localizing radio bursts using the available multispacecraft data. The first method utilizes intensity fitting with a circular Gaussian distribution, while the second method is based on the time arrival of radio bursts. We demonstrate the effectiveness of these methods through the analysis of a single type III burst event and compare their results with the traditional radio triangulation technique. Furthermore, we conduct a statistical study of 17 type III bursts associated with M- and X-class solar flares in years 2020–2022. Our findings suggest a possible correlation between solar flare intensities and longitudes, with east limb flares tending to be weaker than west limb flares. We also observe a systematic drift of radio burst longitudes toward the east, potentially explained by a poleward component of the local density gradient. Our results suggest a strong correlation between solar flare intensities and radio burst properties, enhancing our understanding of the relationship between solar flares and type III radio bursts.

Unified Astronomy Thesaurus concepts: [Radio astronomy \(1338\)](#); [Radio bursts \(1339\)](#); [Solar flares \(1496\)](#)

1. Introduction

Solar radio bursts are a powerful diagnostic tool for understanding the mechanisms of energy release and particle acceleration during solar flares (Wild 1950; Ginzburg & Zhelezniakov 1958). Among these bursts, type III radio bursts are of particular interest, as they provide insights into the propagation of electron beams in the solar corona and interplanetary space (Dulk 2000; Gopalswamy 2011, 2020). These bursts are generated by energetic electron beams traveling outward along open magnetic field lines at velocities close to the speed of light. The localization of type III radio bursts is essential for determining the association between these events and solar flare properties, as well as for understanding the underlying physical processes (Krupar et al. 2014a, 2014b). Bastian et al. (1998) have provided a comprehensive overview of radio emissions produced by solar flares. At frequencies lower than a few megahertz, type III bursts are almost always observed alongside flares that are detected in H α and/or X-rays. In minor flares, specifically A and B class, type III bursts often represent the primary radio emissions associated with these events. In contrast, during more intense flares, such as C, M, and X class, type III bursts generally manifest with enhanced intensity and are frequently detected during the initial stages of the flare impulsive phase (Miteva et al. 2017; Reid & Vilmer 2017). The

flares generally generate several distinct type III bursts at frequencies higher than 10 MHz, which then merge to form a single burst at frequencies lower than 1 MHz.

Recent advancements in multispacecraft missions have provided an unprecedented opportunity to study solar radio bursts from different vantage points (Reiner et al. 2009; Krupar et al. 2020; Musset et al. 2021; Badman et al. 2022). The simultaneous observations from multiple spacecraft offer a unique perspective that can improve the accuracy and reliability of radio burst localization (Martínez Oliveros et al. 2012). Moreover, the combination of data from multiple spacecraft located at different vantage points can reveal new insights into the relationship between radio bursts and solar flares, as well as the underlying physical mechanisms that govern their behavior (Bonnin et al. 2008).

In this study, we utilize data from four widely separated spacecraft, namely Parker Solar Probe, Solar Orbiter, STEREO-A, and Wind, to investigate type III radio bursts and their association with solar flares of magnitude M1.0 and larger. The availability of simultaneous observations from these spacecraft allows us to develop and validate novel methods for localizing radio bursts, improving our understanding of their properties and correlations with solar flares.

In addition to developing these new localization techniques, we also conduct a comprehensive statistical analysis of type III radio bursts associated with M- and X-class solar flares during years 2020–2022. By examining the correlations between solar flare intensities, longitudes, and radio burst properties, we aim to shed



Original content from this work may be used under the terms of the [Creative Commons Attribution 4.0 licence](#). Any further distribution of this work must maintain attribution to the author(s) and the title of the work, journal citation and DOI.

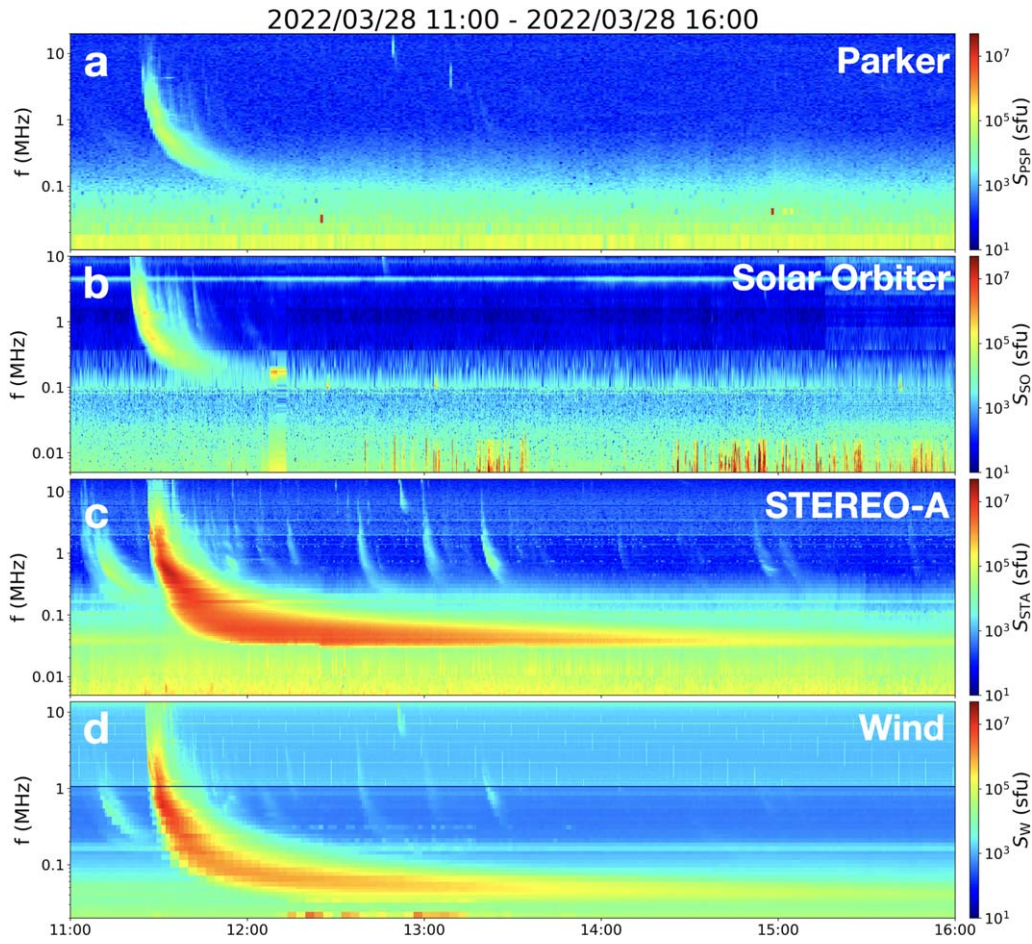


Figure 1. Radio spectra of the type III burst detected on 2022 March 28 by four spacecraft: (a) Parker Solar Probe, (b) Solar Orbiter, (c) STEREO-A, and (d) Wind.

light on the potential factors that influence the behavior of type III radio bursts and their relationship with solar flares.

The structure of this paper is organized as follows. In Section 2, we describe the data and methodology used in this study, focusing on the radio instrument data and presenting a single type III burst example to demonstrate our localization techniques. Section 3 presents the results of our statistical analysis, exploring the correlations between radio bursts and solar flares. In Section 4, we discuss our findings, the implications of our results, and potential directions for future research.

By developing and applying new localization techniques and conducting a comprehensive statistical analysis, our study aims to enhance the current understanding of type III radio bursts and their relationship with solar flares, shedding light on the underlying physical processes and furthering the field of solar radio astronomy.

2. Data and Methodology

In this study, we utilize radio data from four spacecraft: Parker Solar Probe, Solar Orbiter, STEREO-A, and Wind (Russell 1995; Kaiser et al. 2008; Fox et al. 2016; Müller et al. 2020). These spacecraft are equipped with advanced radio instruments that provide high-resolution measurements of type III radio bursts over a wide frequency range (Bougeret et al. 2008, 1995; Bale et al. 2016; Pulupa et al. 2017; Maksimovic et al. 2020; Vecchio et al. 2021; Page et al. 2022). To perform our analysis, we processed radio data from these spacecraft and selected events where type III radio bursts were associated with GOES solar flares included in the

Solar Monitor database⁸ (Gallagher et al. 2002). The combined radio observations from these spacecraft enable us to develop the novel localization methods for estimation of the radio bursts positions and investigate the relationship between radio bursts and solar flares. The data set used in this study covers GOES M- and X-class solar flares during years 2020–2022, when all four spacecraft were operational.

A representative type III burst event observed on 2022 March 28 is shown in Figure 1, demonstrating the radio spectra obtained from the four spacecraft. The radio flux density, measured in solar flux units (sfu), is standardized to a distance of 1 astronomical unit (au) from the Sun (Tapping 2013). This normalization enables us to compare signals measured by spacecraft situated at different distances from the Sun. This particular event was associated with a solar flare class M4.0 located at N14W04 (Figure 2). The solar flare occurred from 10:58 to 11:45, reaching its peak at 11:29. Coincidentally, the associated type III burst also peaked in flux at 1 MHz around 11:29, aligning with the flare’s peak. Given the absence of any other significant type III bursts during the flare duration (i.e., between flare’s start and end times), we are confident in attributing this radio emission to the aforementioned solar flare.

2.1. Localization Techniques

In order to precisely localize type III radio bursts using data from multiple spacecraft, we devised two methods that

⁸ <https://www.solarmonitor.org>

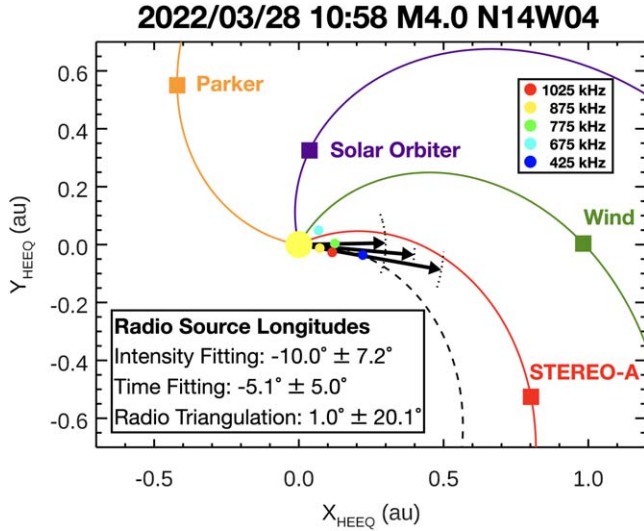


Figure 2. Detailed spatial distribution of spacecraft and radio sources on 2022 March 28 in the HEEQ coordinate system (the $X_{\text{HEEQ}}-Y_{\text{HEEQ}}$ plane). The colored rectangles pinpoint the positions of various spacecraft, with their trajectories illustrated by Parker spirals calculated based on an assumed solar wind speed of 400 km s^{-1} . A particularly notable Parker spiral, originating from the solar flare site at N14W04, is emphasized using a black dashed curve. The triangulated positions of radio sources during this event are marked by distinct colored circles. Three black arrows, differing in length, signify the average azimuths determined by various methods: the longest one represents intensity fitting, the medium-length one corresponds to time-of-arrival fitting, and the shortest one stands for radio triangulation. To provide clarity on the precision of each method, dotted black curves encircle the tips of these arrows, serving as visual representations of the angular error bars.

capitalize on the distinct viewpoints provided by the four spacecraft. The first method, termed intensity fitting, entails analyzing the relative radio peak fluxes for five frequency channels at the four spacecraft (425, 675, 775, 875, and 1025 kHz). The choice of these frequencies is influenced by two factors: Solar Orbiter/RPW/HFR experiences significant electromagnetic perturbations caused mostly by the spacecraft platform and solar panels, resulting in a restricted number of frequency channels suitable for our analysis (refer to Maksimovic et al. 2021 for more information); conversely, Wind/Waves offers calibrated radio flux measurements only up to 1040 kHz. This technique enables us to investigate radio peak fluxes at different frequencies and positions, providing valuable information about the spatial distribution of the radio emission, denoted as $S(\lambda)$. To analyze the radio burst data, we assumed a Gaussian circular distribution, also known as the von Mises distribution (von Mises 1918; Jammalamadaka & SenGupta 2001):

$$S(\lambda) = \frac{S_0}{e^\kappa} e^{\kappa \cos(\lambda - \lambda_0)}, \quad (1)$$

where S_0 is the maximal radio flux, λ_0 is the longitudinal direction of the maximal radio flux, and κ represents the width of the distribution proportional to $\sim \sigma^{-2}$ (a reciprocal measure of dispersion of the von Mises distribution).

In probability theory and directional statistics, the von Mises distribution represents a continuous probability distribution on a circular domain (Risken 1989). This distribution closely approximates the wrapped normal distribution, which serves as the circular counterpart to the standard normal distribution. When an angle λ diffuses freely on a circle, it behaves as a wrapped normally distributed random variable, with its

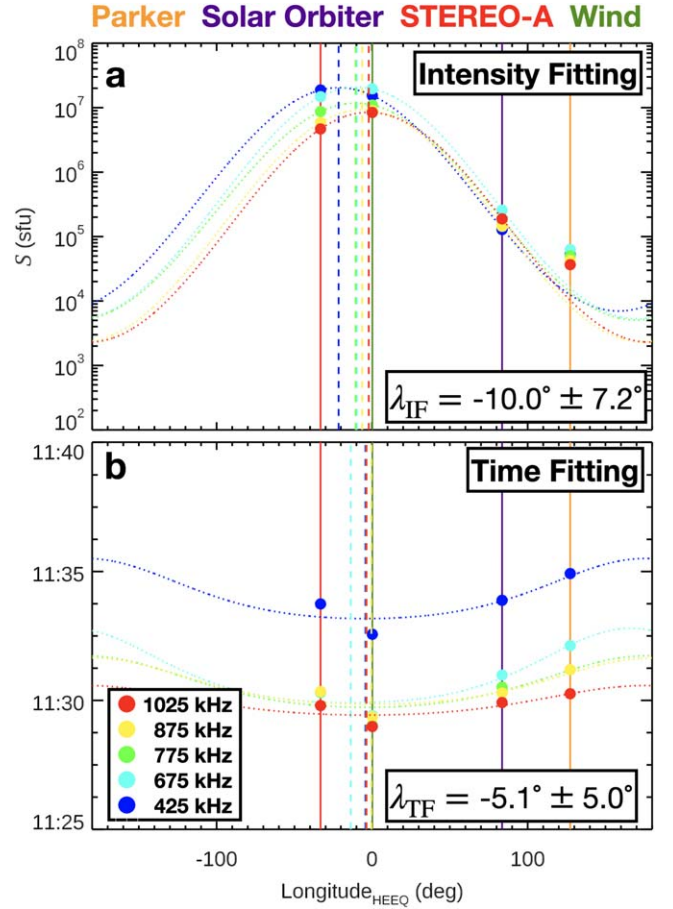


Figure 3. Propagation analysis of the type III burst on 2022 March 28 using intensity and temporal fitting techniques. (a) Radio intensity distribution across spacecraft locations. The intensity of the radio emission for five distinct frequency channels is represented by colored circles, with the corresponding legend provided in panel (b). The positions of the spacecraft at the time of observation are marked by vertical colored lines, with their colors matching those in the figure header. The dotted curves illustrate the fitting results derived from Equation (1), applied individually for each frequency channel. The dashed vertical lines, color-coordinated for clarity, indicate the determined directions for each frequency. These individual directions are then aggregated to compute an average direction, along with its standard deviation, which is displayed in the bottom right corner. (b) Temporal analysis of the type III burst. This panel showcases the timing of the type III burst in relation to the spacecraft's position (Equation (2)), plotted for multiple frequency channels. The characteristics and color-coding remain consistent with the descriptions provided for panel (a).

unwrapped variance increasing linearly over time. Conversely, the von Mises distribution serves as the stationary distribution for a drift and diffusion process occurring on a circle within a harmonic potential, meaning that it exhibits a favored orientation.

By applying this distribution, we were able to identify an average direction λ_0 associated with the maximum flux S_0 , as shown in Figure 3(a). The intensity fitting method produced an angle of $-10.0^\circ \pm 7.2^\circ$, which was computed by averaging the directional values λ_0 obtained for each of the five frequency channels. The accompanying error bars signify the standard deviation obtained from the azimuthal determinations for each frequency. This technique effectively utilizes the available data from the spacecraft to determine the most probable direction of the radio burst source, offering a robust method for localizing radio emissions in space.

The second method we propose relies on the time arrival of radio bursts T_{sc} at five frequency channels at the four spacecraft (Figure 3(b)). For this analysis, the peak flux times T_{sc} were shifted to 1 au:

$$T = T_{sc} + (r_{sc} - 1)c, \quad (2)$$

where r_{sc} is the distance from the Sun to the spacecraft in au and c is the speed of light. This approach exploits the differences in the shifted arrival times of the radio bursts T at each spacecraft to determine the direction of the radio emission where the signal arrives first:

$$T(\lambda) = \frac{T_0}{e^\kappa} e^{\kappa \sin(\lambda - \lambda_0)}, \quad (3)$$

where T_0 is the minimum time, λ_0 is the longitudinal direction of the maximal radio flux, and κ represents the width of the distribution proportional to $\sim \sigma^{-2}$. By identifying a minimum time T_0 corresponding to the radio direction λ_0 , we obtained a value of $-5^\circ.1 \pm 5^\circ.0$ in our example.

Both methods were applied to the type III burst event on 2022 March 28, and their results were compared with the traditional radio triangulation technique using data from STEREO-A and Wind (Krupar et al. 2014a). The triangulation method yielded a direction λ_0 of $1^\circ.0 \pm 20^\circ.1$. While our preliminary comparison of the methods suggests that the two novel approaches may offer localization results with potential accuracy, it is essential to note that this conclusion is based on a single event. The overall accuracy and applicability of these novel methods compared to radio triangulation cannot be firmly established with such a limited data set. A more extensive study is required to thoroughly compare the accuracy of these methods. Importantly, as indicated by Krupar et al. (2012), even instrumental effects in isolation can introduce a deviation of approximately 4° in the wavevector direction. Additionally, it is worth mentioning that Krupar et al. (2014a) demonstrated that radio triangulation provides radio source locations systematically farther from the Sun (5 times for the fundamental emission and 2 times for the harmonic emission), due to radio wave scattering in the solar wind.

In Section 2, we introduced the localization techniques used to determine the source locations of type III radio bursts. These methods are crucial for our analysis, as they allow us to identify where these bursts originate. In Section 3, we will apply these techniques to our data set, comparing the locations of radio bursts with those of solar flares. This comparison aims to understand any potential correlations or patterns between the two phenomena. As we move into Section 3, we will further discuss the results of this analysis using the methods outlined in the previous section.

3. Statistical Results: Radio Bursts and Solar Flares

In this section, we present the results derived from our statistical analysis, emphasizing the associations between type III radio bursts and solar flares of M1.0 class and above. During the period from 2020 to 2022, we studied 83 solar flares, including 74 M-class and 9 X-class events. Of these, 17 events (12 M-class and 5 X-class flares) exhibited a clear association with type III radio bursts. This connection was established temporally, focusing exclusively on those instances where type III bursts detected by Wind transpired within the duration of the flares. Table 1 provides a detailed account of the parameters

pertaining to both the solar flares and their corresponding type III bursts. We note that although some active regions are known to produce numerous solar flares, the 17 events we examined in our study originated from 12 distinct active regions.

Notably, over 50% of type III bursts, specifically 10 events, manifested during the solar flare decay time. In contrast, six events were detected during the solar flare rise time, and a single event was concurrent with the flare's peak. On average, a delay of 0.8 ± 4.9 minutes was noted between the peak of the solar flare and the maximum intensity of the radio emission. This suggests that the type III bursts typically occur in close temporal proximity to the flare's peak.

Benz et al. (2007) examined the relationship between solar flares and radio emissions using ground-based observations ranging from 100 MHz to 4 GHz. Their findings indicate that nearly all flares with a GOES class exceeding C5 are associated with coherent radio emission, provided that they are observed with current sensitivity directly above the source. However, for flares observed at the limb and with a GOES class below M2, the association rate with radio emission drops significantly.

3.1. Localization of Radio Sources

To localize radio sources for the 17 events, we employed the intensity fitting technique discussed in Section 2. The timing method is more sensitive to sufficient spacecraft separation in time (i.e., larger than the time resolution of the radio instruments), and as a result, only a few radio bursts were suitable for application.

Figure 4(a) illustrates the relationship between solar flare intensity and solar flare longitude, denoted by black and red circles. Red color corresponds to solar flares occurring within 45° from Earth's central meridian. In our analysis, we utilized Kendall's τ coefficient to quantify the correlations between various parameters, as it provides a robust and nonparametric measure of association that is less sensitive to outliers and skewed distributions, making it a suitable choice for evaluating the relationships observed in our astrophysical data (Kendall 1938). We observed a correlation between these two quantities: solar flares on the east (negative λ) limb are systematically weaker than solar flares on the west (positive λ) limb (Kendall's τ coefficient of 0.577, principally 100% statistically significant). When we focus solely on events near the central meridian to mitigate potential effects from partial occultation, this correlation persists, evidenced by a Kendall's τ coefficient of 0.491.

In comparing the relationship between solar flare intensity and longitude for flares with and without associated type III bursts, we also conducted an in-depth analysis of flare longitudes over a span of 2 yr. We systematically assessed the intensities in relation to the east-west positions for all M- and X-class solar flares during this period (Figure 4(a)). Utilizing Kendall's τ coefficient, we observed a correlation of 0.217 ± 0.006 . Excluding the flares associated with type III bursts led to a noticeable change in the correlation between flare intensity and longitude, resulting in a revised correlation of 0.124 ± 0.165 . In light of these findings, we surmise that the observed correlation for events associated with radio emissions is not merely coincidental, but rather suggests a potential inherent relationship or characteristic that warrants further exploration. This distinction underscores the intricate relationship between solar flares and their associated type III radio

Table 1
Solar Flares and Type III Bursts

| GOES Class | Date | Solar Flares ^a | | | | | Type III Bursts ^b | | |
|------------|------------|---------------------------|-------|-------|----------------|-------------------|------------------------------|-------|-----------------------------|
| | | Start | Stop | Peak | Position (deg) | NOAA ^c | Radio Flux (sfu) | Peak | Position ^d (deg) |
| M4.4 | 2020-11-29 | 12:34 | 13:41 | 13:11 | S23, E89 | n/a ^e | 3×10^5 | 13:22 | E84 |
| M1.1 | 2021-05-22 | 17:03 | 17:16 | 17:11 | N18, E18 | 2824 | 2×10^5 | 17:12 | E36 |
| M1.1 | 2021-05-23 | 11:00 | 11:14 | 11:08 | N20, E05 | 2824 | 4×10^6 | 11:06 | E23 |
| X1.5 | 2021-07-03 | 14:18 | 14:34 | 14:29 | N23, W82 | 2838 | 1×10^5 | 14:32 | W70 |
| M1.3 | 2021-10-26 | 02:40 | 02:54 | 02:47 | N14, E88 | n/a ^e | 1×10^4 | 02:52 | E81 |
| M1.0 | 2021-10-26 | 15:42 | 16:02 | 15:57 | N13, E89 | n/a ^e | 1×10^4 | 15:56 | E68 |
| X1.0 | 2021-10-28 | 15:17 | 15:48 | 15:35 | S28, W01 | 2887 | 1×10^8 | 15:37 | E03 |
| M1.8 | 2021-12-20 | 11:12 | 11:55 | 11:36 | S20, W01 | 2908 | 2×10^4 | 11:39 | E40 |
| M5.5 | 2022-01-20 | 05:41 | 06:12 | 06:01 | N08, W76 | 2929 | 1×10^7 | 05:58 | W13 |
| M4.0 | 2022-03-28 | 10:58 | 11:45 | 11:29 | N14, W04 | 2975 | 8×10^6 | 11:29 | E10 |
| X1.3 | 2022-03-30 | 17:21 | 17:46 | 17:37 | N13, W31 | 2975 | 1×10^7 | 17:41 | W16 |
| M9.6 | 2022-03-31 | 18:17 | 18:45 | 18:35 | N12, W47 | 2975 | 3×10^5 | 18:42 | W19 |
| X2.2 | 2022-04-20 | 03:41 | 04:04 | 03:57 | S34, W86 | 2992 | 3×10^5 | 03:58 | W75 |
| M6.7 | 2022-08-28 | 15:48 | 16:46 | 16:19 | S30, W85 | 3088 | 2×10^5 | 16:08 | W46 |
| M5.8 | 2022-10-01 | 19:58 | 20:16 | 20:10 | N17, W35 | 3110 | 7×10^5 | 20:05 | W16 |
| X1.0 | 2022-10-02 | 19:53 | 20:34 | 20:25 | N17, W49 | 3110 | 2×10^5 | 20:23 | W22 |
| M3.9 | 2022-10-11 | 08:36 | 08:46 | 08:42 | N24, W35 | 3112 | 2×10^6 | 08:43 | W10 |

Notes.

^a Solar flare parameters from <https://www.solarmonitor.org/>.

^b At 1 MHz from Wind.

^c NOAA active regions are based on the NOAA/USAF Active Region Summary.

^d Derived from intensity fitting.

^e Events not associated with currently named NOAA regions.

bursts, highlighting the need for further in-depth studies in this domain.

Type IV radio bursts arise from electrons trapped in the post-eruption arcades that follow coronal mass ejections (CMEs; Gopalswamy 2011). Sakurai (1973) analyzed wide-band type IV solar radio bursts, focusing on the onset time differences between microwave and metric frequencies and their correlation with the longitudinal positions of associated solar flares on the solar disk. The study by Sakurai (1973) revealed that the peak flux intensity is at its zenith when flares are located 10° – 40° west of the solar disk’s central meridian. This observation is attributed to the nonuniform expansion of magnetic bottles that ensnare mildly relativistic electrons, the culprits behind type IV bursts. The expansion pattern suggests that these bottles tend to shift 10° – 30° eastward from the meridian plane intersecting the flare regions. In a more contemporary study, Gopalswamy et al. (2016) observed that type IV bursts radiate within a narrow cone (spanning less than $\sim 60^\circ$ in width) above the flare site, implying that observers must be positioned within a relatively narrow angle to capture the entirety of the burst.

While solar flares are expected to be uniformly distributed in longitude, this significant deviation in those associated with type III bursts can be attributed to the Parker spiral geometry (Parker 1958). This finding implies that the spatial distribution of solar flares plays a significant role in determining the characteristics of the associated type III radio bursts. The correlation may be influenced by several factors, such as variations in the magnetic field strength and topology, the density of the plasma in the solar corona, and the efficiency of the electron acceleration process in different regions of the Sun. The discerned association between solar flare intensity and its position might be rooted in certain magnetic field configurations being more adept at generating electron beams.

Next, we compared solar flare longitudes with radio burst longitudes obtained from intensity fitting (Figure 4(b)). We observed a systematic drift toward the east by $17^\circ.65 \pm 1^\circ.86$. The uncertainty in the eastward drift stems from the linear fitting, represented as the standard deviation of the resulting parameter. The observed drift may be indicative of an eastward shift in the longitude diagram. We speculate that this shift could potentially be linked to a poleward component of the local density gradient along the type III electron open-field tube. This might result in a refractive index gradient, which could then bend radiation equatorward. Bonnin et al. (2008) observed such systematic drift toward the east by 23° between 740 and 940 kHz in the Wind and Ulysses data.

3.2. Correlations between Radio Burst Properties and Solar Flare Characteristics

To elucidate the relationship between radio bursts and solar flares, we probed the correlations of radio flux at Wind (a spacecraft proximate to Earth) with solar flare intensity and also between radio burst longitude and flare intensity. As depicted in Figure 5(a), the radio flux at Wind varies as a function of flare intensity. A moderate correlation is evident (Kendall’s τ_{45} coefficient of 0.473, approximately 78% significant) for flares within 45° of the central meridian (highlighted in red). However, this correlation wanes when considering all flares ($\tau_{90} = 0.207 \pm 0.245$).

Figure 5(b) illustrates the association between radio burst longitude and solar flare intensity. A marked correlation emerges (Kendall’s τ_{90} coefficient of 0.652, nearly 100% significant) across all data points, both black and red. This trend indicates that the associated solar flares exhibit heightened intensity toward the west limb, aligning with observations from Figure 4(a). When narrowing the scope to

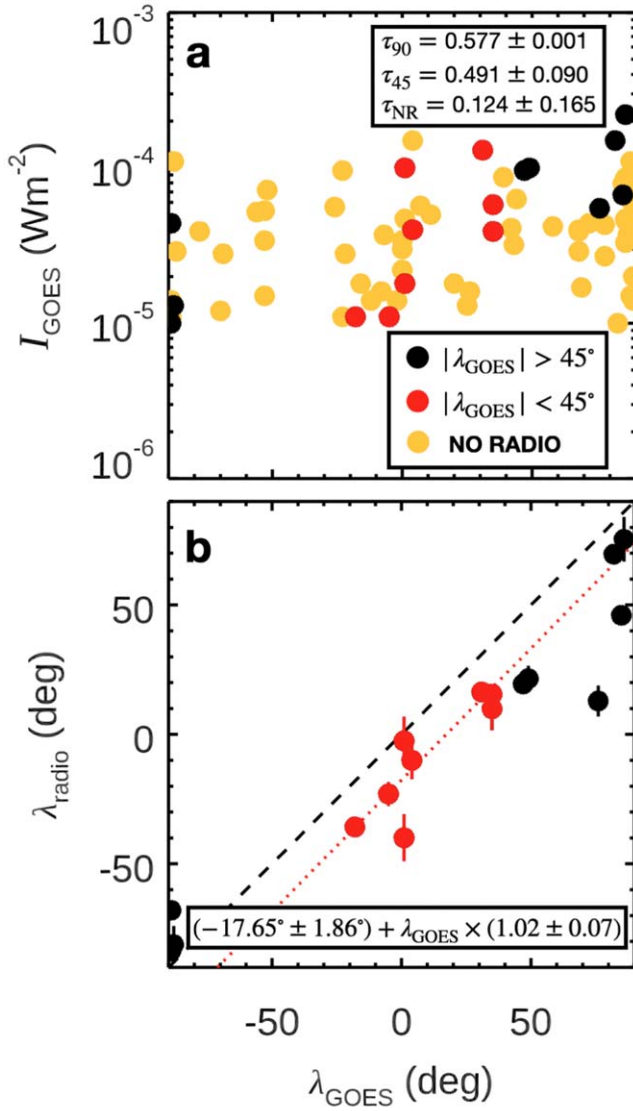


Figure 4. Statistical analysis of 17 type III bursts in association with solar flares. (a) Solar flare intensity and longitude relationship. This plot showcases solar flare intensity as a function of its longitude. Black and red circles represent the observed solar flares, with the red circles specifically highlighting flares that are within 45° of the central meridian, allowing for a clear distinction between limb and central meridian flares. The Kendall's correlation coefficient, τ_{90} , is computed for the entire data set (both black and red circles), while τ_{45} is specifically derived for the red circles. Yellow circles denote solar flares unaccompanied by type III radio bursts within the corresponding time interval, for which we computed the coefficient τ_{NR} . (b) Longitude correlation of solar flares and radio bursts. This panel juxtaposes the longitudes of solar flares against those of the associated type III radio bursts, as determined by the intensity fitting method. A noticeable systematic eastward shift of 17° is evident, based on the linear fitting of the red circles. This fitting result is visually represented by the red dotted line.

flares within 45° , the correlation slightly decreases yet remains significant ($\tau_{45} = 0.618 \pm 0.032$).

In Figure 5(c), we delve into an in-depth exploration of the relationship between the speed of the type III burst beam and the intensity of solar flares. Our current localization methodology, grounded in intensity fitting, excels in deducing the direction of the radio burst propagation. However, it presents a challenge when it comes to estimating the speed of the electron beam involved in the burst. Recognizing this limitation, we turned to an established empirical electron density model

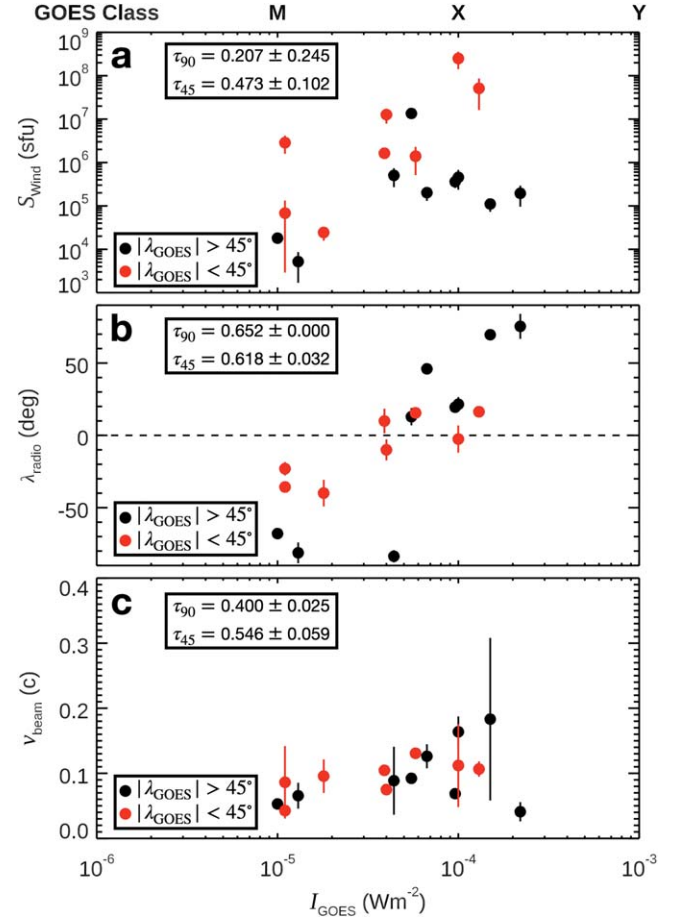


Figure 5. Statistical analysis of 17 type III bursts in association with solar flares. (a) Radio flux and solar flare intensity relationship. This panel displays the radio flux observed by the Wind spacecraft plotted against the solar flare intensity. The notation follows the conventions established in Figure 4(a). (b) Longitude correlation with solar flare intensity. This panel presents the longitude of the radio burst as a function of solar flare intensity. A pronounced correlation is evident, underscoring the relationship between the spatial position of the burst and the flare's intensity. (c) Beam speed and solar flare intensity dynamics. Here the speed of the type III burst beam is plotted against the solar flare intensity. The observed correlation suggests that electron beams with higher velocities tend to be associated with more intense solar flares. Error bars represent the standard deviation derived from a multifrequency analysis.

proposed by Sittler & Guhathakurta (1999). This model provides a framework for translating observed frequencies into radial distances from the Sun, thereby offering indirect insights into the beam's speed.

Upon analyzing the data, a pattern emerged. The red data points, in particular, exhibit a significant Kendall correlation of $\tau_{45} = 0.546 \pm 0.059$. This implies that more intense solar flares, with their heightened energy release, are often associated with electron beams that propagate at faster speeds. Such a trend aligns with the intuitive hypothesis that larger energy discharges from potent flares would drive electron beams with greater velocities. However, it is noteworthy that when the analysis is expanded to encompass the entire data set, this correlation shows a degree of attenuation, settling at $\tau_{90} = 0.400 \pm 0.025$. This slight diminution suggests potential factors or intricacies at play that warrant further investigation.

3.3. Implications of the Statistical Analysis

Our statistical analysis sheds light on the intricate interplay between type III radio bursts and solar flares. The observed

correlations among solar flare intensities, longitudes, and specific radio burst attributes point to underlying physical mechanisms shaping the dynamics of type III radio bursts in conjunction with solar flares.

Notably, the systematic variance observed in both solar flare intensities and longitudes, complemented by the consistent eastward shift in radio burst longitudes, underscores the significance of accounting for the Parker spiral geometry and the local density gradient in type III radio burst studies. Radio wave propagation is linked to the local plasma density, which is influenced by the magnetic field lines guiding the plasma. Although radio waves themselves are not directly altered by the magnetic fields, the plasma through which they travel is affected. This plasma, shaped and directed by magnetic fields, forms pathways that control the movement of electrons. As these electrons follow the magnetic trajectories, they bring about variations in the plasma density. These changes in density consequently impact the propagation of radio waves. This interaction is key to understanding why radio emissions, such as type III radio bursts, often mirror the configurations of the Parker spiral. Essentially, while radio waves are immune to the direct effects of magnetic fields, their propagation is indirectly influenced by the plasma density variations induced by electron movements along these fields. Additionally, the pronounced correlation between the intensities of solar flares and specific properties of radio bursts underscores the pivotal roles of both energy release during solar flares and particle acceleration in shaping the observed radio patterns.

However, it is worth noting that the observed correlation between solar flare intensity and longitude aligns with the “big flare syndrome,” a phenomenon where more energetic solar flares are typically accompanied by a variety of other intense solar activities, such as larger sunspot groups, stronger CMEs, and more powerful radio bursts (Kahler 1982). This association further highlights the complex interplay between various solar phenomena and their potential combined influence on space weather.

Our findings also imply that the localization of type III radio bursts is critical for understanding the connections between these events and solar flare properties. The novel localization techniques developed in this study, which take advantage of the unique vantage points provided by multiple spacecraft, have the potential to significantly improve our understanding of these relationships and the underlying physical mechanisms, such as scattering of radio waves due to solar wind turbulence (Kontar et al. 2017, 2019; Krupar et al. 2018).

Furthermore, the observed correlation between type III burst beam speed and solar flare intensity suggests that the strength of solar flares may play a role in determining the speed of electron beams associated with type III radio bursts. This finding could have important implications for our understanding of the particle acceleration processes in the solar corona and the factors that govern the propagation of electron beams in interplanetary space (Reid & Ratcliffe 2014).

Overall, the results of our statistical analysis underscore the value of multispacecraft observations for studying type III radio bursts and their association with solar flares. By leveraging these observations and developing new localization techniques, our study contributes to a more comprehensive understanding of the complex relationships between radio bursts, solar flares, and the physical processes that drive their behavior (Cane et al. 2002).

4. Conclusions

In this study, we have presented an innovative approach to localizing type III radio bursts using multispacecraft observations from Parker Solar Probe, Solar Orbiter, STEREO-A, and Wind. We introduced two localization methods and demonstrated their effectiveness by comparing their results with those obtained from the traditional radio triangulation technique. Our findings highlight the potential of using widely separated spacecraft to accurately track radio bursts and study their associations with solar flares.

Our rigorous statistical analysis, focusing on type III radio bursts in conjunction with solar flares of magnitude M1.0 and above, has brought to light pivotal correlations. Notably, we discerned that solar flares associated with type III bursts emanating from the east limb are generally less intense than their counterparts from the west limb.

Additionally, we observe an eastward shift in radio burst longitudes. However, we recognize that this observation, primarily based on a subset of data, may not fully represent the complexity of the phenomena. The apparent drift could be influenced by a poleward component within the local density gradient, operating alongside the type III electron open-field tube.

In parallel, our study has pinpointed robust correlations between the intensity of solar flares and certain properties of radio bursts, like the radio flux recorded at Wind and the longitudinal coordinates of radio bursts. Our analysis reveals a noteworthy correlation between the speed of type III burst beams and the intensity of solar flares. While this correlation is of interest, we recognize that it might be influenced by factors such as the “big flare syndrome,” which could affect the relationships between solar flare intensities and certain properties of radio bursts. This observation, therefore, should be considered as one aspect of our broader findings, meriting further investigation to fully understand its implications.

In conclusion, our study demonstrates the value of multispacecraft observations for studying type III radio bursts and their associations with solar flares. By developing and applying new localization techniques, we contribute to a more comprehensive understanding of the complex relationships between radio bursts, solar flares, and the physical processes that drive their behavior. Future studies could benefit from incorporating additional observational data, such as in situ plasma measurements and high-resolution imaging, to further enhance our understanding of type III radio bursts and their connections to solar activity.

Acknowledgments

Parker Solar Probe was designed, built, and is now operated by the Johns Hopkins Applied Physics Laboratory as part of NASA’s Living with a Star (LWS) program (contract NNN06AA01C). Support from the LWS management and technical team has played a critical role in the success of the Parker Solar Probe mission. The FIELDS instrument suite was designed and built and is operated by a consortium of institutions including the University of California, Berkeley, University of Minnesota, University of Colorado, Boulder, NASA/GSFC, CNRS/LPC2E, University of New Hampshire, University of Maryland, UCLA, IFRU, Observatoire de Meudon, Imperial College, London, and Queen Mary University of London. Solar Orbiter is a space mission of

international collaboration between ESA and NASA, operated by ESA. The authors would like to thank the many individuals and institutions who contributed to making STEREO and Wind possible. V.K. was supported by the STEREO/Waves and Wind/Waves projects, and by the NASA grant 19-HSR-19_2-0143. Radio data are publicly available at <https://spdf.gsfc.nasa.gov/> (Parker, Solar Orbiter and STEREO-A) and <https://cdpp-archive.cnes.fr> (Wind). Solar flare data supplied courtesy of <https://www.solarmonitor.org>.

ORCID iDs

Vratislav Krupar  <https://orcid.org/0000-0001-6185-3945>
 Oksana Kruparova  <https://orcid.org/0000-0002-1122-6422>
 Adam Szabo  <https://orcid.org/0000-0003-3255-9071>
 Frantisek Nemec  <https://orcid.org/0000-0002-3233-2718>
 Milan Maksimovic  <https://orcid.org/0000-0001-6172-5062>
 Juan Carlos Martinez Oliveros  <https://orcid.org/0000-0002-2587-1342>
 David Lario  <https://orcid.org/0000-0002-3176-8704>
 Xavier Bonnin  <https://orcid.org/0000-0003-4217-7333>
 Antonio Vecchio  <https://orcid.org/0000-0002-2002-1701>
 Marc Pulupa  <https://orcid.org/0000-0002-1573-7457>
 Stuart D. Bale  <https://orcid.org/0000-0002-1989-3596>

References

Badman, S. T., Carley, E., Cañizares, L. A., et al. 2022, *ApJ*, **938**, 95
 Bale, S. D., Goetz, K., Harvey, P. R., et al. 2016, *SSRv*, **204**, 49
 Bastian, T. S., Benz, A. O., & Gary, D. E. 1998, *ARA&A*, **36**, 131
 Benz, A. O., Brajša, R., & Magdalenic, J. 2007, *SoPh*, **240**, 263
 Bonnin, X., Hoang, S., & Maksimovic, M. 2008, *A&A*, **489**, 419
 Bougeret, J. L., Goetz, K., Kaiser, M. L., et al. 2008, *SSRv*, **136**, 487
 Bougeret, J. L., Kaiser, M. L., Kellogg, P. J., et al. 1995, *SSRv*, **71**, 231
 Cane, H. V., Erickson, W. C., & Prestage, N. P. 2002, *JGRA*, **107**, 1315
 Dulk, G. A. 2000, *GMS*, **119**, 115
 Fox, N. J., Velli, M. C., Bale, S. D., et al. 2016, *SSRv*, **204**, 7

Gallagher, P. T., Moon, Y. J., & Wang, H. 2002, *SoPh*, **209**, 171
 Ginzburg, V. L., & Zhelezniakov, V. V. 1958, *SvA*, **2**, 653
 Gopalswamy, N. 2011, in Proc. of the 7th Int. Workshop on Planetary, Solar and Heliospheric Emissions, ed. H. O. Rucker et al. (Vienna: Austrian Academy of Sciences Press), 325
 Gopalswamy, N. 2020, arXiv:2008.09222
 Gopalswamy, N., Akiyama, S., Mäkelä, P., Yashiro, S., & Cairns, I. H. 2016, arXiv:1605.02223
 Jammalamadaka, S. R., & SenGupta, A. 2001, Topics in Circular Statistics (Singapore: World Scientific)
 Kahler, S. W. 1982, *JGR*, **87**, 3439
 Kaiser, M. L., Kucera, T. A., Davila, J. M., et al. 2008, *SSRv*, **136**, 5
 Kendall, M. G. 1938, *Biometrika*, **30**, 81
 Kontar, E. P., Chen, X., Chrysaphi, N., et al. 2019, *ApJ*, **884**, 122
 Kontar, E. P., Yu, S., Kuznetsov, A. A., et al. 2017, *NatCo*, **8**, 1515
 Krupar, V., Maksimovic, M., Kontar, E. P., et al. 2018, *ApJ*, **857**, 82
 Krupar, V., Maksimovic, M., Santolik, O., Cecconi, B., & Kruparova, O. 2014a, *SoPh*, **289**, 4633
 Krupar, V., Maksimovic, M., Santolik, O., et al. 2014b, *SoPh*, **289**, 3121
 Krupar, V., Santolik, O., Cecconi, B., et al. 2012, *JGRA*, **117**, A06101
 Krupar, V., Szabo, A., Maksimovic, M., et al. 2020, *ApJS*, **246**, 57
 Maksimovic, M., Bale, S. D., Chust, T., et al. 2020, *A&A*, **642**, A12
 Maksimovic, M., Souček, J., Chust, T., et al. 2021, *A&A*, **656**, A41
 Martínez Oliveros, J. C., Raftery, C. L., Bain, H. M., et al. 2012, *ApJ*, **748**, 66
 Miteva, R., Samwel, S. W., & Krupar, V. 2017, *JSWSC*, **7**, A37
 Müller, D., Cyr, O. C., St., Zouganelis, I., et al. 2020, *A&A*, **642**, A1
 Musset, S., Maksimovic, M., Kontar, E., et al. 2021, *A&A*, **656**, A34
 Page, B., Bassett, N., Lecacheux, A., et al. 2022, *A&A*, **668**, A127
 Parker, E. N. 1958, *ApJ*, **128**, 664
 Pulupa, M., Bale, S. D., Bonnell, J. W., et al. 2017, *JGRA*, **122**, 2836
 Reid, H. A. S., & Ratcliffe, H. 2014, *RAA*, **14**, 773
 Reid, H. A. S., & Vilmer, N. 2017, *A&A*, **597**, A77
 Reiner, M. J., Goetz, K., Fainberg, J., et al. 2009, *SoPh*, **259**, 255
 Risken, H. 1989, The Fokker-Planck Equation. Methods of Solution and Applications (Berlin: Springer)
 Russell, C. T. 1995, The Global Geospace Mission (Dordrecht: Kluwer)
 Sakurai, K. 1973, *SoPh*, **31**, 483
 Sittler, E. C., Jr., & Guhathakurta, M. 1999, *ApJ*, **523**, 812
 Tapping, K. F. 2013, *SpWea*, **11**, 394
 Vecchio, A., Maksimovic, M., Krupar, V., et al. 2021, *A&A*, **656**, A33
 von Mises, R. 1918, *PhyZ*, **19**, 490
 Wild, J. P. 1950, *AuSRA*, **3**, 541